Journal of the Optical Society of America A
OPTICS, IMAGE SCIENCE, AND VISION

Diagonal illumination scheme for Fourier ptychographic microscopy: resolution doubling and aliasing minimization

YEFENG SHU,[1,2,3,†] JIASONG SUN,[1,2,3,†] YAO FAN,[1,2,3] YAO JIN,[1,2,3] QIAN CHEN,[1,2,3] AND CHAO ZUO[1,2,3,*]

[1]Smart Computational Imaging Laboratory (SCILab), School of Electronic and Optical Engineering, Nanjing University of Science and Technology, Nanjing, Jiangsu Province 210094, China
[2]Smart Computational Imaging Research Institute (SCIRI) of Nanjing University of Science and Technology, Nanjing, Jiangsu Province 210019, China
[3]Jiangsu Key Laboratory of Spectral Imaging & Intelligent Sense, Nanjing, Jiangsu Province 210094, China
[†]These authors contributed equally to this work.
*zuochao@njust.edu.cn

Received 5 July 2024; revised 11 September 2024; accepted 11 September 2024; posted 16 September 2024; published 4 October 2024

Fourier ptychographic microscopy (FPM) is a high-throughput computational imaging technology that enables wide-field and high-resolution imaging of samples with both amplitude and phase information. It holds great promise for quantitative phase imaging (QPI) on a large population of cells in parallel. However, detector undersampling leads to spectrum aliasing, which may significantly degenerate the resolution, efficiency, and quality of QPI, especially when an objective lens with a high space–bandwidth product is used. Here, we introduce a diagonal illumination scheme for FPM to minimize spectrum aliasing, enabling high-resolution QPI under a limited detector sampling rate. By orienting the LED illumination diagonally relative to the detector plane, the non-aliased sampling frequency of the raw image under oblique illumination can be maximized. This illumination scheme, when integrated with a color camera, facilitates single-shot, high-throughput QPI, effectively overcoming spectrum aliasing and achieving incoherent diffraction-limited resolution. Theoretical analysis, simulations, and experiments on resolution target and live cells validate the effectiveness and the proposed illumination scheme, offering a potential guideline for designing an FPM platform for high-speed QPI under the limited detector sampling rates.

https://doi.org/10.1364/JOSAA.532252

1. INTRODUCTION

Quantitative phase imaging (QPI) enables objective measure of cell morphology and dynamics in a label-free way, which is invaluable for biomedical research [1]. However, QPI has long been achieved through laser-based interferometry; consequently, the imaging quality is inevitably compromised by system instability and intrinsic speckle noise introduced by the coherent source. To overcome these challenges, Gabriel Popescu (affectionately known as Gabi) is a pioneer to develop QPI technologies with robust interferometry and broad-band source. In 2006, diffraction phase microscopy (DPM) [2] invented by Gabi realized robust common-path interferometric phase imaging, which aroused wide concern. So far, DPM has been widely adopted by biological laboratories worldwide through adding a compact optical module on existing microscopes. In the proposed spatial light interference microscopy (SLIM) [3] in 2010, Gabi realized phase-shift interferometric phase imaging using a white light source based on a commercial phase-contrast microscope. The technology of SLIM allows high-contrast imaging on subcellular structures of high signal-to-noise ratio. Further, SLIM is applied in tomographic microscopy to reveal three-dimensional structures of biological cells [4]. In 2017, Gabi invented gradient light interference microcopy (GLIM) [5] through combining common-path interferometry with differential interference contrast (DIC) microscopy. The invented GLIM achieves excellent sectioning for volume imaging on thick tissues. Compared with high-coherent interferometric QPI, the adopted partially coherent source in Gabi's common-path interferometry revolutionarily improves the phase imaging quality. The success of these technologies greatly inspired the later development of non-interferometric computational phase microscopy [6–12]. Sharing the same intention with Gabi, these technologies enable robust observation and avoid speckle noise of laser sources. Furthermore, they additionally offer

advantages such as simple hardware implementation, efficient synthetic aperture, high imaging throughput, and system error self-calibration.

As a typical computational phase imaging technology, Fourier ptychographic microscopy (FPM) surpasses the resolution limit of a low-magnification objective lens and realizes high-resolution complex amplitude imaging across a large FOV [13,14]. Specifically, the low-resolution images encoded with phase information and high-frequency components are captured via angular illumination scanning and are synthesized together in the Fourier domain for supper-resolution based on the principle of synthetic aperture [15] and phase retrieval [16,17]. In this way, the inherent space–bandwidth product (SBP) limit of the optical imaging system is circumvented, enabling high-throughput QPI to simultaneously record large populations of cells as well as subcellular structures [18–20]. It is significant for live-cell research, including drug discovery, cancer cell biology, and personalized genomics [21,22].

A common problem in FPM is the spectrum aliasing caused by the undersampling of a detector that will seriously degrade imaging quality. According to the Nyquist sampling theorem, the detector sampling rate should be at least two times the cutoff frequency of the signal to be measured [23]. Through the derivation of the optical transfer function (OTF) [24], it is known that the maximum cutoff frequency of the captured intensity image in FPM can achieve twice the coherent diffraction limit. Therefore, the minimum detector sampling rate required to avoid spectrum aliasing is determined. It should be noted that the spectrum aliasing problem is hard to be avoided in some cases, especially when adopting the objective lens with high SBP. For example, for a coherent imaging system using the objective lens with NA of 0.4 and magnification of 10×, spectrum aliasing occurs easily as the camera pixel size is larger than ∼5 μm. In this condition, the digital imaging resolution is limited by the pixel size of the detector but is not the resolution theoretically achievable for the optical system. Meanwhile, the artifacts in reconstruction results caused by spectrum aliasing are non-negligible and will make resolved details unreliable [25].

As a kind of state mixture [26–28], it is known that the aliased spectrum can be solved in an algorithm through ptychographic reconstruction for pixel superresolution [29,30]. Specifically, an upsampled scheme [27,31] has been demonstrated to be crucial for successful spectrum de-aliasing, where a pixel binning procedure is added in the forward generation of low-resolution intensity images in the algorithm. However, it should be noted that the successful spectrum de-aliasing in FPM requires additional raw intensity images to promise adequate data redundancy [31]. It means that the problem of spectrum aliasing is solved at the expense of sacrificing imaging efficiency. It is not achievable for real-time *in vitro* applications, where the total exposure is expected to be short to record fast subcellular dynamics without motion blur. Several versions of sparse [30–32] or multiplexing [19,33,34] LED illumination schemes are developed to reduce the captured raw images. As probably the fastest FPM technology for high-speed phase imaging, the annular illumination satisfying an NA-matched illumination condition allows accurate phase characterization using at least 4–6 intensity images [24,35,36]. In these conditions where only a few images are captured per frame of live-cell imaging, the problem of spectrum aliasing could not be solved under existing frameworks.

In this paper, we present an optimal illumination scheme for FPM to improve the high-speed phase imaging quality under spectrum aliasing, which is induced by the undersampling of the detector. It is known that the detector samples the optical image more densely in the diagonal direction [37]. Here, we adopt a diagonal illumination mode (i.e., the illumination direction is diagonal at detector plane) for the minimization of spectrum aliasing and achieve high-quality phase reconstruction not requiring additional intensity images. In our demonstration of the proposed diagonal illumination scheme, two orthogonal LEDs are lit simultaneously to realize a single-shot QPI, combined with a color camera. Two monochromatic intensity images of different illumination directions at each color channel are separated and used to realize phase recovery of incoherent diffraction-limited resolution under a pure-phase object assumption. In general, the proposed diagonal illumination scheme enables a high spatio-temporal resolution imaging, simultaneously minimizing the effect of spectrum aliasing.

2. SPECTRUM ALIASING PROBLEM OF FPM UNDER MATCHED ILLUMINATION

The optical transfer function (OTF) characterizes the relationship between the system's intensity response and the sample's complex field in the frequency domain under the weak object assumption. The cutoff frequency of the OTF is simultaneously decided by the numerical aperture of the objective lens (NA_{obj}) and the spatiotemporal coherence of the illumination source [38]. In the case of tilted coherent illumination, the OTF of the system comprises two shifted anti-symmetric pupils that are subtracted or added to one another, corresponding respectively to the phase and absorption responses of the sample [24]. The phase OTF is cut off in the low-frequency region because the two pupils cancel each other out. The phenomenon can only be avoided when the NA of illumination equals NA_{obj}, which is called the matched illumination condition [39,40]. Therefore, the matched illumination is adopted as a necessary illumination scheme for accurate phase characterization in FPM. Meanwhile, the optical resolution of the recovered phase image reaches the incoherent diffraction limit (twice the coherent diffraction limit, $f_{obj} = NA_{obj}/\lambda$) in this condition. To completely record the optical information transferred by the microscope under matched illumination condition, the detector sampling rate should be properly selected to satisfy the Nyquist sampling theorem, which should be at least twice the signal's maximum frequency. The detector sampling rate is decided by the pixel size (Δ) and magnification of the imaging system (Mag), which is defined as $f_{cam} = 2\Delta/Mag$. To determine whether the detector sampling rate is sufficient for the optical imaging system, a spatial sampling rate is defined as

$$R_{cam} = \frac{f_{cam}}{f_{obj}} = \frac{\lambda}{NA_{obj}} \frac{Mag}{2\Delta}. \tag{1}$$

When R_{cam} equals 2, it can be seen in Fig. 1(a) that the OTF is exactly included within the detector cutoff frequency. It indicates that the detector can record the full frequency components

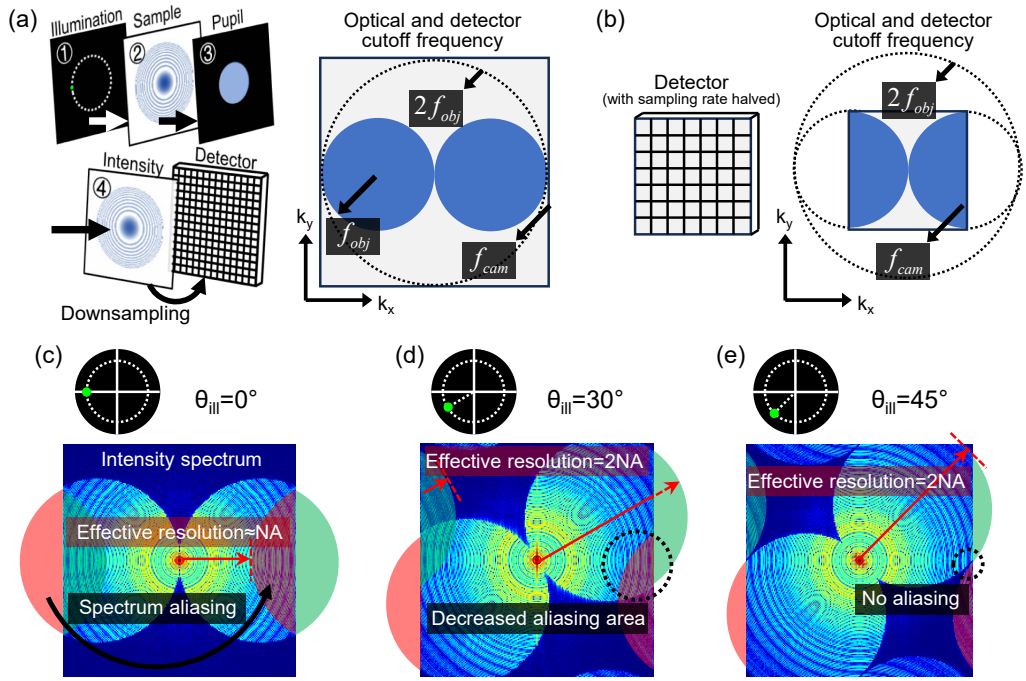

Fig. 1. Spectrum aliasing problem of FPM under matched illumination. (a) Process of optical imaging and detector sampling, and the resultant cutoff frequency in Fourier domain. (b) The halving of the sampling rate results in part of the optical information exceeding the detector cutoff frequency. (c)–(e) Fourier spectra of intensity images under matched illumination of varying directions (0°, 30°, and 45°).

of the intensity image under the matched illumination. For another case in Fig. 1(b), as the detector sampling rate is reduced by two, it can be seen that only half of the frequency components can be sampled by the detector. Generally, R_{cam} is required to be at least 2 under the matched illumination for the normal cases given above to satisfy the Nyquist criterion. We also observe that the spectrum of the image is not isotropic and achieves the maximum frequency in the diagonal direction due to the fact that the detector units are arranged line by line. It provides the potential to alleviate the undersampling problem through properly selecting the illumination direction to maximize the collection of the sample's spectrum.

We illustrate the effect of illumination direction on the sampling process of the detector through examples presented in Figs. 1(c)–1(e). The spatial sampling rate R_{cam} is set to $\sqrt{2}$. When the direction angle is 0°, the spectral component that exceeds the detector cutoff frequency (represented by the red and green regions) can be regarded as having shifted from one side to another, resulting in an overlap with the unshifted components. The phenomenon is called spectrum aliasing [23]. In this condition, the effective NA is decreased from 2NA to ∼1NA, which is due to the fact that the aliased spectrum will cause artifacts on the reconstructed image and makes the resolved frequency component exceeding 1NA not reliable, as shown in Fig. 1(c). As the direction is changed to 30°, the overlapping area between the shifted and unshifted spectral component becomes smaller, which indicates that less spectrum is aliased in this condition. It can be observed that part of the high-frequency spectrum exceeds the detector cutoff frequency but is not aliased with the unshifted spectral component. This part of high-frequency information can be easily restored in reconstruction, as it is merely shifted rather than aliased. Hence the effective NA actually reaches 2NA. As the direction angle equals 45° shown in Fig. 1(e), it can be observed that there is no aliased area in the spectrum. In this condition, the detector's sampling rate can be maximumly utilized to record optical information, thereby completely circumventing the problem of spectrum aliasing.

3. ANALYSIS OF SPECTRUM ALIASING IN RELATION TO ILLUMINATION DIRECTION AND OBJECTIVE LENS SELECTION

The potential that the spectrum aliasing problem can be mitigated through properly selecting the illumination direction of the LED has been demonstrated. As a more in-depth exploration for the optimal illumination scheme under spectrum aliasing, we further quantitatively investigated the effect of illumination directions under different spatial sampling rates. Three typical Olympus high-SBP objective lens with different magnifications (10×, 20×, and 40×) are selected for the more practical demonstration. The LED illumination wavelength and detector pixel size are setted as the commonly used parameters of 550 nm and 6.5 μm for the calculation of the spatial sampling rate of the three objective lenses. Exact parameters of the objective lens and corresponding spatial sampling rates are provided in Table 1.

We quantify the extent of spectrum aliasing by introducing a metric known as spectrum aliasing rate, which is defined as the ratio of aliased area to total area of OTF. Several example diagrams are provided in Figs. 2(a)–2(c) to visualize the aliased

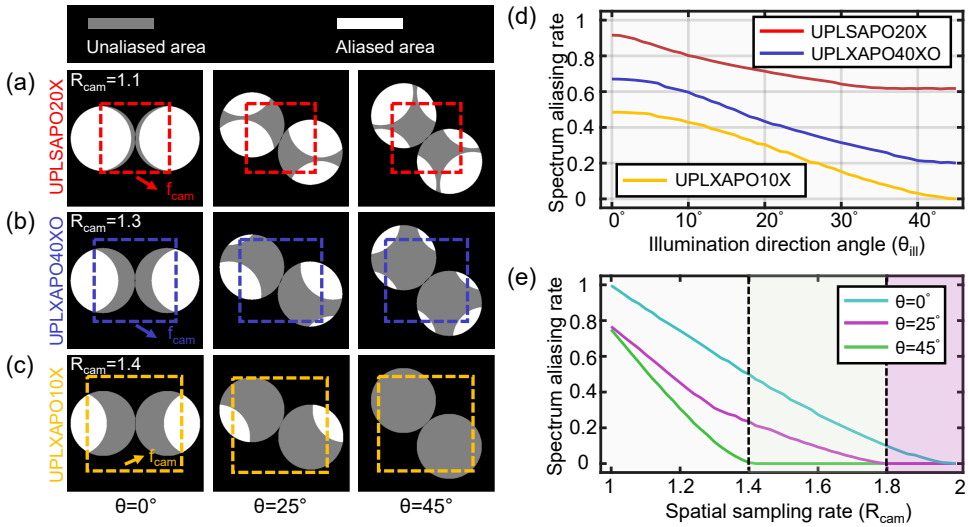

Fig. 2. Analysis of spectrum aliasing in relation to illumination direction and objective lens selection. (a)–(c) Spectrum aliasing rate schematic diagrams of three objective lenses under illumination directions of 0°, 25°, and 45°. (d) Curves of spectrum aliasing rate with illumination direction angle for the three objective lenses. (e) Curves of spectrum aliasing rate with spatial sampling rate under illumination directions of 0°, 25°, and 45°.

Table 1. Key Parameters of Three Commonly Used High-SBP Objective Lenses and Corresponding Spatial Sampling Rates at Illumination Wavelength of 550 nm and Detector Pixel Size of 6.5 μm

Objective Lens	*Mag*	NA_{obj}	R_{cam}
UPLFLN10X2	10×	0.3	≈ 1.4
UPLSAPO20X	20×	0.75	≈ 1.1
UPLXAPO40XO	40×	1.35	≈ 1.3
$\lambda = 550$ nm	$\Delta = 6.5$ μm		

OTFs of the three objective lenses under the illumination directions of $\theta = 0°, \theta = 25°$, and $\theta = 45°$. The white and gray parts separately denote the area with and without aliasing. The dotted boxes on the diagrams denote the cutoff frequency of the detector. Figure 2(d) shows a more specific line chart demonstrating the relationships of spectrum aliasing rate with illumination direction for the three objective lenses. The analysis of the diagrams and line chart indicates that all three objective lenses exhibit a consistent trend: the spectrum aliasing rate decreases as the illumination direction varies from 0° to 45°, reaching its minimum at 45°, or known as diagonal illumination. However, it should be noted that for the 10× objective lens with the sampling rate $R_{cam} = 1.1$, spectrum aliasing remains a significant issue even under the diagonal illumination. It indicates that more intensity images are unavoidably required for de-aliasing in algorithm. Meanwhile, for the remaining two objective lenses with $R_{cam} = 1.3$ and $R_{cam} = 1.4$, the aliasing problem can almost be completely avoided if adopting the diagonal illumination. It indicates that no more intensity images are required to solve the spectrum aliasing problem, which facilitates the high-speed phase imaging only collecting a few images per frame. The examples on the three representative objective lenses indicate that the diagonal illumination is the optimal illumination direction for minimizing the spectrum aliasing, but it still cannot completely avoid the problem as the spatial sampling rate is low. Hence, we further explore its applicable range. We give the relationship between spectrum aliasing rate and spatial sampling rate under illumination direction of 0°, 25°, and 45°, respectively, as shown in Fig. 2(e). It is found that at least 2, 1.8, and 1.4 of spatial sampling rates are required for completely avoiding spectrum aliasing under illumination directions of 0°, 25°, and 45°, respectively. It indicates that the spatial sampling rate of 1.4 is the critical threshold that must be adhered to in the selection of the experimental parameter to avoid the spectrum aliasing problem.

4. SINGLE-SHOT PHASE RETRIEVAL UNDER DIAGONAL ILLUMINATION SCHEME AND THEORETICAL SIMULATION VALIDATION

It has been established that the diagonal illumination can serve as an optimal scheme for FPM to effectively minimize spectrum aliasing. Here, we will demonstrate how to enable a single-shot QPI that maximumly utilizes the camera sampling rate under a diagonal color-multiplexed illumination scheme. We simultaneously illuminate the sample with both a red and a green LED and capture the raw image using a color camera, as shown in Fig. 3(a). The monochromatic intensity images of two illumination directions are acquired through separately extracting the red and the green channels from the color image. Further, as illustrated in Figs. 3(b) and 3(c), the intensity images corresponding to opposite illumination directions can be generated through a straightforward computational approach:

$$I_G = 2\bar{I}_C - I_C, \tag{2}$$

where I_G is the generated intensity image, I_C is the experimentally captured intensity image, and $\bar{I}_C$ is the mean value of the captured intensity image. The calculation is based on the principle that the phase contrast of opposite illumination direction is inverse, which is derived from the phase transfer function of FPM [24]. Hence, if a pure-phase object assumption is imposed, the intensity of opposite illumination direction can

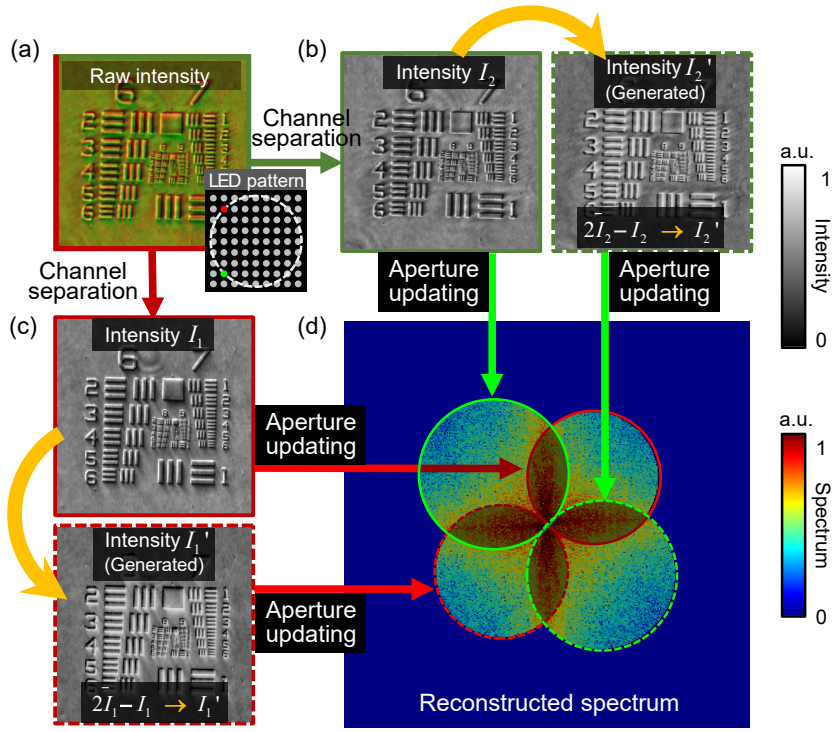

Fig. 3. Updating the four centrosymmetric apertures in spectrum using one captured intensity image under pure-phase object assumption. (a) Truly captured intensity image. (b),(c) Two monochromatic images (I_1, I_2) separated from an RGB image and two processed images (I_1', I_2') generated from I_1 and I_2. (d) Reconstructed spectrum, where the four centrosymmetric apertures are updated by the intensity images in (b) and (c).

be obtained through overturning the contrast and keeping the direct component unchanged. In this way, totally four apertures can be alternatively updated in reconstruction using two captured images and two generated images [see Fig. 3(d)]. In our previous work, it has been demonstrated that a set of four images have sufficient data redundancy to achieve a quasi-isotropic spectral coverage after the reconstruction [24,35]. The updating procedure for a single aperture follows a typical FPM algorithm framework [13]. It should be emphasized that an upsampled scheme [31] is crucial to promise a successful spectral de-aliasing in phase retrieval under limited detector sampling rate; otherwise, significant artifacts may arise. The reconstructed phase map is continuously refined through the updating of four apertures until the convergence condition is satisfied.

In order to validate the advantage of the diagonal illumination scheme under limited detector sampling rate, we performed simulations under four LED illumination modes for comparison as shown in Fig. 4. In simulations, we adopted a 10×, 0.3NA objective lens, and the wavelength of LED illumination and detector pixel size were set as 550 nm and 6.5 μm. The corresponding spatial sampling rate R_{cam} is 1.4 in this condition, which is within the rage where the spectrum aliasing could be completely avoided if adopting the diagonal illumination scheme, as is discussed in Section 3. To testify to the effect of spectrum aliasing on reconstructed results, a pure-phase Siemens Star (with phase height of 1 rad) was adopted as the sample for simulation. In Fig. 4, we provide the illumination diagram of four representative illumination modes, as well as the corresponding effective Fourier support, recovered Fourier spectra, and phase maps. The coverage of the Fourier support is decided by the sum of apertures used in iterative reconstruction [see circular regions in Fig. 4(a), 4(c), and 4(d)] and is also determined by the pixel resolution of the detector under the condition of spectrum aliasing [see square region in Fig. 4(b)]. The first group of results in Fig. 4(a) was reconstructed using 12 annular-distributed LEDs selected from the LED array, which satisfy the matched illumination condition. Considering the adequate data redundancy and spectral coverage, the reconstructed phase map in Fig. 4(a) can be seen as the standard result closest to ground truth. In Fig. 4(b), the number of adopted LEDs was reduced to 4 under an orthogonal illumination scheme. Due to the fact that the aliased spectral component was not correctly solved in this condition, the effective resolution of the reconstructed result was limited within the detector cutoff frequency. Therefore, the obtained phase resolution was significantly reduced compared with Fig. 4(a) and was accompanied with noticeable artifacts, as shown in Figs. 4(b) and 4(e). In Fig. 4(c), we applied the diagonal illumination scheme to select four LEDs for phase reconstruction. It can be seen that the artifact was suppressed compared with Fig. 4(b), and the recovered resolution was almost identical to the result in Fig. 4(a). Although the spectrum in Fig. 4(a) exhibits closer to an isotropic distribution compared to that shown in Fig. 4(c), the difference of the two reconstructed phase maps is almost indistinguishable. The same conclusion can be obtained through the comparison of phase profiles in Fig. 4(e). Finally, we demonstrated the results of adopting the single-shot imaging scheme. The other wavelength for multiplexing imaging was set to be 630 nm. It can be observed that the reconstructed phase map were almost identical to Figs. 4(a) and 4(c). Hence, a successful single-shot QPI with

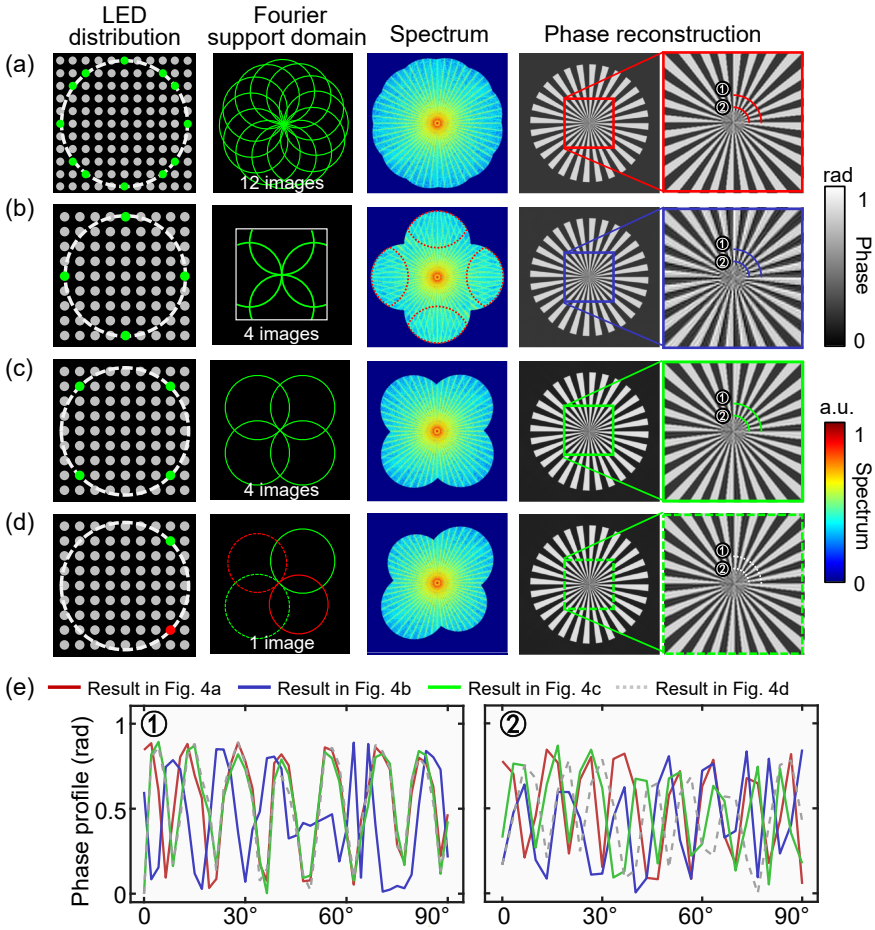

Fig. 4. Simulation of phase retrieval under different LED illumination modes. (a) Results reconstructed with 12 LED elements in an array satisfying the matched illumination condition, including the effective Fourier support, reconstructed spectrum and phase map. (b) Results reconstructed with four LED elements of the illumination directions with 0°, 90°, 180°, and 270°. (c) Results reconstructed with four LEDs under diagonal illuminations. (d) Results reconstructed with two LEDs under diagonal illuminations and single-shot imaging. (e) Comparison of circular phase profiles in (a)–(d) with two radii.

spectra de-aliasing has been demonstrated under the diagonal illumination scheme.

5. EXPERIMENTAL RESULTS

In order to verify the effectiveness of the proposed method, the experiment was performed on a USAF1951 pure-phase resolution target. An Olympus IX73 microscope was used for microscopic imaging. A objective lens with a magnification of 10 (OLYMPUS, PlanN10X, 0.25NA) and a SCMOS camera (HAMAMASTU, ORCA-Flash 4.0, 2048 × 2048 pixels) were used. The detector pixel size is 6.5 μm. The full-FOV reconstructed phase map of 1.77 mm × 1.77 mm is provided in Fig. 5(a), as well as a zoomed-in phase map visualizing Groups 6 and 7. Figure 5(b) shows the corresponding intensity images under illumination direction of 0° and 45°. A smaller subregion was selected from the full FOV for the comparison of reconstruction resolution under different conditions. For the first set S1, when red light was used for illumination (the central wavelength is 632 nm) under the illumination direction of 0°, the quantitative phase imaging results, the enlarged subregion, and the reconstructed Fourier spectrum are shown in Fig. 5(c). For the second set S2, keeping the illumination directions of the four LEDs unchanged, and switching to blue light illumination (the central wavelength is 460 nm), the reconstruction results are shown in Fig. 5(d). For the third set S3, when blue light was used, the illumination directions were adjusted to 45°. Considering the measured sample is the transparent object, the raw images used are reduced from 4 to 2 according to pure-phase object assumption, as demonstrated in Section 4. The reconstruction results are shown in Fig. 5(e). From these three sets of comparative experiments, it can be seen that when the illumination wavelength is 632 nm, the spatial sampling rate $R_{\text{cam}} = 1.945 \approx 2$, which almost satisfies the Nyquist sampling theorem under incoherent illumination, so there is no distortion in the reconstruction results [see Fig. 5(a)], and the smallest resolvable element of Group 9 Element 5 (615 nm) also reaches the theoretical highest half-width resolution (632 nm). When the illumination direction is not changed and only the illumination wavelength is reduced to 430 nm, the spatial sampling rate $R_{\text{cam}} = 1.32 < 2$, which no longer satisfies the Nyquist sampling theorem under incoherent illumination. So, the reconstructed phase distribution has been severely distorted on the Group 9 Elements 4–6 [see Fig. 5(d)]. Through simply

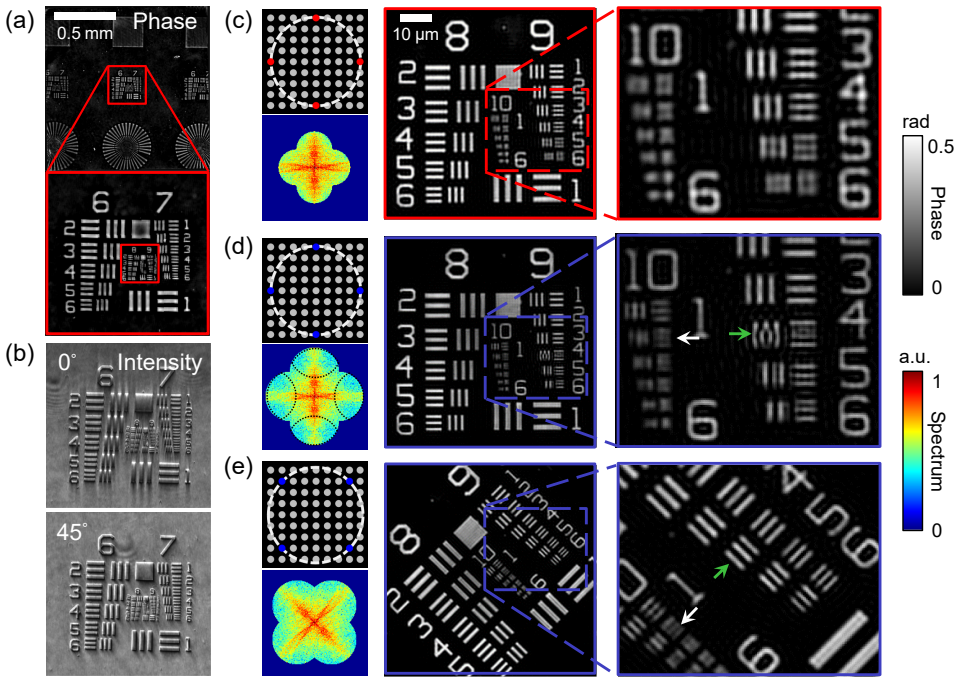

Fig. 5. Experimental results on USAF-1951 quantitative phase resolution target. (a) Full FOV of reconstructed phase map imaged by a 10×, 0.25NA objective lens. (b) Raw intensity images with illumination directions of 0° and 45°. (c) Zoomed-in phase map reconstructed from intensity with 632 nm illumination wavelength and 0° illumination direction. (d) Zoomed-in phase map reconstructed from intensity with 430 nm illumination wavelength and 0° illumination direction. (e) Zoomed-in phase map reconstructed from intensity with 430 nm illumination wavelength and 45° illumination direction.

adjusting illumination directions of the LEDs, the imaging resolution and artifacts have been significantly improved, as shown in Fig. 5(e). At the 430 nm illumination wavelength, it can be seen that the distortion in Fig. 5(d) has completely disappeared. The smallest resolvable element is Group 10 Element 2 (435 nm), which almost reaches the theoretical half-width resolution (430 nm). Here, the phase resolution target in Fig. 5(e) was rotated by 45° to eliminate the effects of anisotropic imaging resolution for a fair comparison.

To further demonstrate that the proposed illumination scheme can achieve the optimal live-cell phase imaging quality in the presence of spectrum aliasing, we performed dynamic imaging of human hepatocellular carcinoma cells using a high-SBP objective lens (OLYMPUS, UPLSAPO20X, 0.75NA), as shown in Fig. 6. The raw images were captured at a frame rate of 10 Hz. Figure 6(a) shows four phase images of a single cell cut from 20× full-FOV images at intervals of 3 min. It can be observed that the morphology of the cell was gradually shrinking, which was probably caused by the unsuited culture environment. Figures 6(b) and 6(c) show the reconstructed phase images under diagonal and orthogonal illumination schemes, respectively, which are zoomed in from Fig. 6(a) for more clear visualization. It can be seen that the reconstruction results under diagonal illumination in Fig. 6(b) exhibit significantly better than orthogonal illumination in Fig. 6(c), as the lipid droplets are closer to circular shapes, which are consistent with the published results. To highlight the difference of the two groups of reconstructed results, the phase profiles of the first and last frames in Figs. 6(b) and 6(c) are provided. In these profiles, it can be seen that higher resolution was achieved with reconstruction under diagonal illumination compared to that under orthogonal illumination. The diagrams of spectrum aliasing explain this phenomenon, which indicates that much fewer high-frequency components in spectrum are aliased under diagonal illumination. Additionally, we also compare reconstruction results using more intensity images under the annular matched illumination. From the spectra of reconstructed phase maps, it can be observed that the better isotropic resolution can be achieved when performing the reconstruction using 8 and 20 intensity images. However, the difference is negligible in the comparison of phase profiles. In general, it can be concluded from our presented results that the diagonal illumination scheme can minimize the effect of spectrum aliasing and achieve incoherent diffraction-limited phase imaging resolution under a single exposure. The results reconstructed from few raw images have been demonstrated to be equivalent to the results with more raw images. The full video recording morphological variation of the live cell in Fig. 6 for 27 min is provided in Visualization 1, which gives a dynamic comparison on reconstructed results of different imaging schemes.

6. CONCLUSION AND DISCUSSION

In general, we propose a diagonal illumination scheme to cope with the problem of spectrum aliasing in FPM on the condition of not additionally acquiring raw images. The spectrum aliasing occurs when the optical image is undersampled by the detector according to the Nyquist sampling theorem. Owing to the fact that detector units are arranged line by line, the frequency domain of an image is anisotropic and achieves the highest

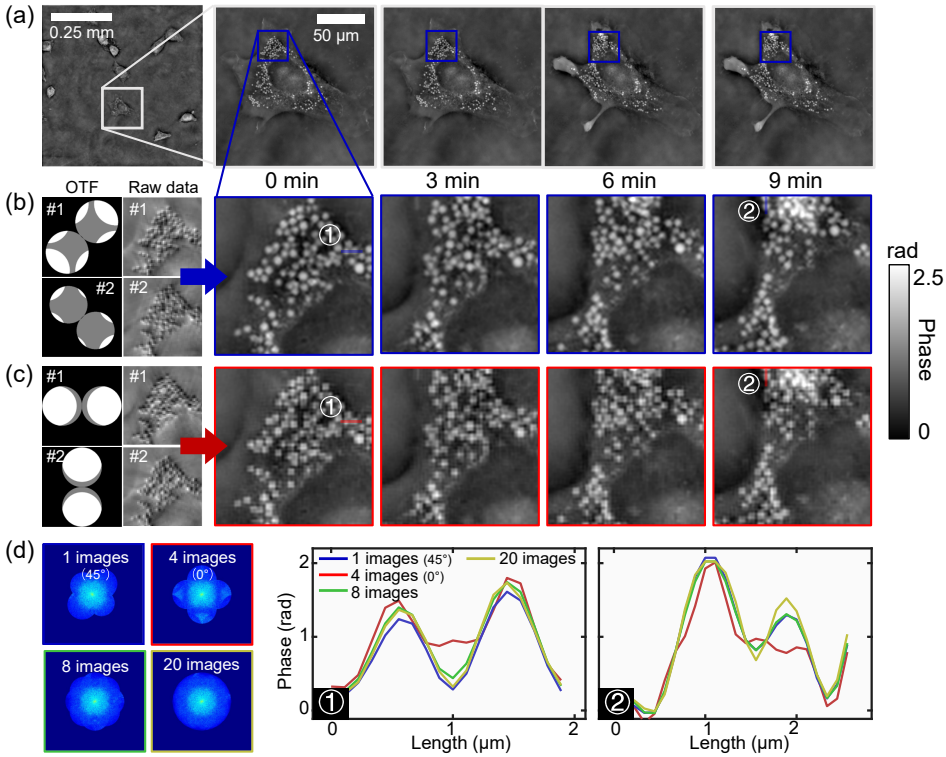

Fig. 6. Experimental results on living cells (human hepatocellular carcinoma cell, PLC/REF/5). (a) Four frames of phase map in different times for a human hepatocellular carcinoma cell cut from the FOV of a 20×, 0.75NA objective lens, which are reconstructed under single-shot diagonal illumination scheme. (b) Enlarged phase maps of area of interest (ROI) in (a), as well as the spectrum aliasing diagram. (c) Phase maps of comparison with (b) reconstructed from four intensity images with LED illumination direction of 0°. (d) Comparison of phase profiles reconstructed with four annular illumination schemes, as well as the corresponding reconstruction spectra.

sampling frequency in the diagonal direction. Through setting the orientation of the OTF to be diagonal in the frequency domain by the proposed illumination scheme, the optical image transmitted by the microscope can be maximumly sampled where the spectrum aliasing area is minimized. The effectiveness of diagonal illumination scheme is also quantitatively validated in the line charts of Figs. 2(d) and 2(e). It is known that the spectrum aliasing can be solved in algorithm through ptychographic reconstruction; however, it additionally requires much more raw images to promise adequate data redundancy. The same challenge in lens-free microscopy has to be overcome through lateral-shifted pixel super-resolution [41], multi-angle illumination [42], and wavelength scanning [43], requiring extra modulations that are costly in both time and hardware. Here, through applying the diagonal illumination scheme, only two images are required to realize the dynamic phase imaging achieving incoherent diffraction-limited resolution under limited detector sampling rate, which is a much more simple and efficient way. Furthermore, the implementation of the diagonal illumination scheme permits the use of detectors with larger pixel size for capturing raw images. Usually, the larger pixel size of charge coupled devices (CCDs) or complementary metal–oxide-semiconductor (CMOS) correlates with higher performance parameters, including dynamic range, frame rate, and quantum efficiency. These improvements facilitate higher phase imaging sensitivity and speed.

Although the diagonal illumination scheme has been validated to maximumly exploit the Fourier domain of the detector in FPM, it should be noted that the spectrum aliasing cannot be completely avoided when the detector sampling rate is lower than a threshold value [specifically, when $R_{\mathrm{cam}} < 1.4$; see Fig. 2(e)]. This means that the spectrum is seriously aliased in these conditions, and, inevitably, more raw images are required or the system parameters (i.e., magnification, NA, and detector pixel size) should be redesigned to completely recover the sample's high-frequency information. Meanwhile, if performing reconstruction on raw intensity images with unavoidable aliasing as shown in Fig. 6 when $R_{\mathrm{cam}} = 1.1$, the imaging results under diagonal illumination still perform much better than orthogonal illumination [see Figs. 6(b) and 6(c)]. In addition, it is important to emphasize that the methodology and theoretical framework presented in this article rely on a fundamental assumption known as the weak object assumption. The weak object assumption is introduced to linearize the imaging process and is the basis to derive the transfer function. The assumption is valid on most of the thin samples, such as adherent cells. For the thick samples which are multiple-scattering, we notice that the spectrum of intensity under tilt illumination exhibits a similar distribution characteristic with thin sample [44], although there are still some spectrum components exceeding the support of the transfer function. Hence, it can be concluded that the diagonal illumination scheme is also applicable for the thick samples. Furthermore, we mainly analyze the aliasing problem here for

bright-field imaging under matched illumination condition, where the spectrum is mainly composed of linear parts (i.e., the two circular components; see Fig. 1). For the dark-field imaging in FPM, the spectrum is composed of non-linear components [45]; hence it is worth exploring to develop an imaging scheme to minimize spectrum aliasing in this condition and whether the diagonal illumination remains a viable solution to addressing the aliasing problem.

Funding. National Natural Science Foundation of China (62105151, 62175109, 62227818, 62361136588, U21B2033); National Key Research and Development Program of China (2022YFA1205002, 2024YFE0101300); Leading Technology of Jiangsu Basic Research Plan (BK20192003); Youth Foundation of Jiangsu Province (BK20210338); Biomedical Competition Foundation of Jiangsu Province (BE2022847); Key National Industrial Technology Cooperation Foundation of Jiangsu Province (BZ2022039); Fundamental Research Funds for the Central Universities (2023102001, 30920032101, 30923010206); Open Research Fund of Jiangsu Key Laboratory of Spectral Imaging Intelligent Sense (JSGP202105, JSGP202201).

Acknowledgment. I, Chao Zuo, wish to express my heartfelt gratitude and share my deep sorrow for the loss of Gabi, a giant in the field of QPI, whose pioneering work has not only significantly advanced the frontiers of optical imaging but also opened new avenues for exploring the intricacies of biological specimens in a label-free manner. Gabi has long been a beacon of inspiration for me, not just through his published research but also through the personal interactions that I was fortunate enough to have with him. The legacy that Gabi leaves behind transcends the scholarly pages of scientific journals and resonates in the hearts and minds of all whom he influenced. His impact will continue to ripple through the optics and biophotonics community, inspiring us to push the boundaries of what is possible in QPI and beyond.

Disclosures. The authors declare no conflicts of interest.

Data availability. The data that support the findings of this study are available from the corresponding author upon reasonable request.

REFERENCES

1. Y. Park, C. Depeursinge, and G. Popescu, "Quantitative phase imaging in biomedicine," Nat. Photonics **12**, 578–589 (2018).
2. G. Popescu, T. Ikeda, R. R. Dasari, *et al.*, "Diffraction phase microscopy for quantifying cell structure and dynamics," Opt. Lett. **31**, 775–777 (2006).
3. Z. Wang, L. Millet, M. Mir, *et al.*, "Spatial light interference microscopy (SLIM)," Opt. Express **19**, 1016–1026 (2011).
4. T. Kim, R. Zhou, M. Mir, *et al.*, "White-light diffraction tomography of unlabelled live cells," Nat. Photonics **8**, 256–263 (2014).
5. T. H. Nguyen, M. E. Kandel, M. Rubessa, *et al.*, "Gradient light interference microscopy for 3D imaging of unlabeled specimens," Nat. Commun. **8**, 210 (2017).
6. X. Ou, G. Zheng, and C. Yang, "Embedded pupil function recovery for Fourier ptychographic microscopy," Opt. Express **22**, 4960–4972 (2014).
7. L. Tian and L. Waller, "3D intensity and phase imaging from light field measurements in an led array microscope," Optica **2**, 104–111 (2015).
8. L. Tian and L. Waller, "Quantitative differential phase contrast imaging in an led array microscope," Opt. Express **23**, 11394–11403 (2015).
9. J. Sun, Q. Chen, Y. Zhang, *et al.*, "Efficient positional misalignment correction method for fourier ptychographic microscopy," Biomed. Opt. Express **7**, 1336–1350 (2016).
10. C. Zuo, J. Sun, J. Li, *et al.*, "High-resolution transport-of-intensity quantitative phase microscopy with annular illumination," Sci. Rep. **7**, 7654 (2017).
11. Y. Baek and Y. Park, "Intensity-based holographic imaging via space-domain Kramers–Kronig relations," Nat. Photonics **15**, 354–360 (2021).
12. Y. Fan, J. Li, L. Lu, *et al.*, "Smart computational light microscopes (SCLMS) of smart computational imaging laboratory (SCILAB)," PhotoniX **2**, 1–64 (2021).
13. G. Zheng, R. Horstmeyer, and C. Yang, "Wide-field, high-resolution Fourier ptychographic microscopy," Nat. Photonics **7**, 739–745 (2013).
14. S. Jiang, P. Song, T. Wang, *et al.*, "Spatial-and Fourier-domain ptychography for high-throughput bio-imaging," Nat. Protoc. **18**, 2051–2083 (2023).
15. V. Mico, Z. Zalevsky, P. Garca-Martnez, *et al.*, "Synthetic aperture superresolution with multiple off-axis holograms," J. Opt. Soc. Am. A **23**, 3162–3170 (2006).
16. J. R. Fienup, "Phase retrieval algorithms: a comparison," Appl. Opt. **21**, 2758–2769 (1982).
17. X. Chang, L. Bian, and J. Zhang, "Large-scale phase retrieval," eLight **1**, 4 (2021).
18. X. Ou, R. Horstmeyer, C. Yang, *et al.*, "Quantitative phase imaging via Fourier ptychographic microscopy," Opt. Lett. **38**, 4845–4848 (2013).
19. L. Tian, Z. Liu, L.-H. Yeh, *et al.*, "Computational illumination for high-speed in vitro Fourier ptychographic microscopy," Optica **2**, 904–911 (2015).
20. C. Zuo, J. Sun, J. Li, *et al.*, "Wide-field high-resolution 3D microscopy with Fourier ptychographic diffraction tomography," Opt. Laser Eng. **128**, 106003 (2020).
21. E. Glory and R. F. Murphy, "Automated subcellular location determination and high-throughput microscopy," Dev. Cell **12**, 7–16 (2007).
22. V. Starkuviene and R. Pepperkok, "The potential of high-content high-throughput microscopy in drug discovery," Br. J. Pharmacology **152**, 62–71 (2007).
23. H. Landau, "Sampling, data transmission, and the Nyquist rate," Proc. IEEE **55**, 1701–1706 (1967).
24. J. Sun, C. Zuo, J. Zhang, *et al.*, "High-speed Fourier ptychographic microscopy based on programmable annular illuminations," Sci. Rep. **8**, 7669 (2018).
25. K. Guo, S. Dong, and G. Zheng, "Fourier ptychography for brightfield, phase, darkfield, reflective, multi-slice, and fluorescence imaging," IEEE J. Sel. Top. Quantum Electron. **22**, 77–88 (2015).
26. P. Thibault and A. Menzel, "Reconstructing state mixtures from diffraction measurements," Nature **494**, 68–71 (2013).
27. D. Batey, T. Edo, C. Rau, *et al.*, "Reciprocal-space up-sampling from real-space oversampling in x-ray ptychography," Phys. Rev. A **89**, 043812 (2014).
28. D. J. Batey, D. Claus, and J. M. Rodenburg, "Information multiplexing in ptychography," Ultramicroscopy **138**, 13–21 (2014).
29. S. Dong, R. Horstmeyer, R. Shiradkar, *et al.*, "Aperture-scanning Fourier ptychography for 3D refocusing and super-resolution macroscopic imaging," Opt. Express **22**, 13586–13599 (2014).
30. S. Dong, Z. Bian, R. Shiradkar, *et al.*, "Sparsely sampled Fourier ptychography," Opt. Express **22**, 5455–5464 (2014).
31. J. Sun, Q. Chen, Y. Zhang, *et al.*, "Sampling criteria for Fourier ptychographic microscopy in object space and frequency space," Opt. Express **24**, 15765–15781 (2016).
32. S. Zhou, J. Li, J. Sun, *et al.*, "Accelerated Fourier ptychographic diffraction tomography with sparse annular led illuminations," J. Biophoton. **15**, e202100272 (2022).
33. L. Tian, X. Li, K. Ramchandran, *et al.*, "Multiplexed coded illumination for Fourier ptychography with an led array microscope," Biomed. Opt. Express **5**, 2376–2389 (2014).
34. Y. Fan, J. Sun, Y. Shu, *et al.*, "Efficient synthetic aperture for phaseless Fourier ptychographic microscopy with hybrid coherent and incoherent illumination," Laser Photon. Rev. **17**, 2200201 (2023).
35. J. Sun, Q. Chen, J. Zhang, *et al.*, "Single-shot quantitative phase microscopy based on color-multiplexed Fourier ptychography," Opt. Lett. **43**, 3365–3368 (2018).
36. Y. Shu, J. Sun, J. Lyu, *et al.*, "Adaptive optical quantitative phase imaging based on annular illumination Fourier ptychographic microscopy," PhotoniX **3**, 24 (2022).
37. S. Jiang, M. Guan, J. Wu, *et al.*, "Frequency-domain diagonal extension imaging," Adv. Photon. **2**, 1 (2020).

38. C. Zuo, J. Li, J. Sun, *et al.*, "Transport of intensity equation: a tutorial," Opt. Laser Eng. **135**, 106187 (2020).
39. S. Zhou, J. Li, J. Sun, *et al.*, "Transport-of-intensity Fourier ptychographic diffraction tomography: defying the matched illumination condition," Optica **9**, 1362–1373 (2022).
40. J. Li, N. Zhou, J. Sun, *et al.*, "Transport of intensity diffraction tomography with non-interferometric synthetic aperture for three-dimensional label-free microscopy," Light Sci. Appl. **11**, 154 (2022).
41. W. Bishara, T.-W. Su, A. F. Coskun, *et al.*, "Lensfree on-chip microscopy over a wide field-of-view using pixel super-resolution," Opt. Express **18**, 11181–11191 (2010).
42. G. Zheng, S. A. Lee, Y. Antebi, *et al.*, "The epetri dish, an on-chip cell imaging platform based on subpixel perspective sweeping microscopy (SPSM)," Proc. Natl. Acad. Sci. USA **108**, 16889–16894 (2011).
43. X. Wu, J. Sun, J. Zhang, *et al.*, "Wavelength-scanning lensfree on-chip microscopy for wide-field pixel-super-resolved quantitative phase imaging," Opt. Lett. **46**, 2023–2026 (2021).
44. S. Chowdhury, M. Chen, R. Eckert, *et al.*, "High-resolution 3D refractive index microscopy of multiple-scattering samples from intensity images," Optica **6**, 1211–1219 (2019).
45. R. Cao, C. Shen, and C. Yang, "High-resolution, large field-of-view label-free imaging via aberration-corrected, closed-form complex field reconstruction," Nat. Commun. **15**, 4713 (2024).